BEILSTEIN JOURNAL OF NANOTECHNOLOGY

# Fabrication of $CeO_2$–$MO_x$ (M = Cu, Co, Ni) composite yolk–shell nanospheres with enhanced catalytic properties for CO oxidation

Ling Liu[*1,2], Jingjing Shi[3], Hongxia Cao[3], Ruiyu Wang[1,2] and Ziwu Liu[*1]

Full Research Paper

Open Access

Address:
[1]Low Carbon Energy Institute, China University of Mining and Technology, Xuzhou 221008, People's Republic of China, [2]Key Laboratory of Coal-Based CO2 Capture and Geological Storage of Jiangsu Province, China University of Mining and Technology, Xuzhou 221008, People's Republic of China and [3]School of Chemical Engineering and Technology, China University of Mining and Technology, Xuzhou 221116, People's Republic of China

Email:
Ling Liu[*] - liuling@cumt.edu.cn; Ziwu Liu[*] - lzwmsy@cumt.edu.cn

* Corresponding author

Keywords:
$CeO_2$; CO oxidation; surface decoration; synergistic interaction; yolk–shell structure

*Beilstein J. Nanotechnol.* **2017,** *8,* 2425–2437.
doi:10.3762/bjnano.8.241

Received: 04 May 2017
Accepted: 23 October 2017
Published: 16 November 2017

Associate Editor: R. Xu

© 2017 Liu et al.; licensee Beilstein-Institut.
License and terms: see end of document.

## Abstract

$CeO_2$–$MO_x$ (M = Cu, Co, Ni) composite yolk–shell nanospheres with uniform size were fabricated by a general wet-chemical approach. It involved a non-equilibrium heat-treatment of Ce coordination polymer colloidal spheres (Ce-CPCSs) with a proper heating rate to produce $CeO_2$ yolk–shell nanospheres, followed by a solvothermal treatment of as-synthesized $CeO_2$ with $M(CH_3COO)_2$ in ethanol solution. During the solvothermal process, highly dispersed $MO_x$ species were decorated on the surface of $CeO_2$ yolk–shell nanospheres to form $CeO_2$–$MO_x$ composites. As a CO oxidation catalyst, the $CeO_2$–$MO_x$ composite yolk–shell nanospheres showed strikingly higher catalytic activity than naked $CeO_2$ due to the strong synergistic interaction at the interface sites between $MO_x$ and $CeO_2$. Cycling tests demonstrate the good cycle stability of these yolk–shell nanospheres. The initial concentration of $M(CH_3COO)_2{\cdot}xH_2O$ in the synthesis process played a significant role in catalytic performance for CO oxidation. Impressively, complete CO conversion as reached at a relatively low temperature of 145 °C over the $CeO_2$–$CuO_x$-2 sample. Furthermore, the $CeO_2$–$CuO_x$ catalyst is more active than the $CeO_2$–$CoO_x$ and $CeO_2$–NiO catalysts, indicating that the catalytic activity is correlates with the metal oxide. Additionally, this versatile synthesis approach can be expected to create other ceria-based composite oxide systems with various structures for a broad range of technical applications.

## Introduction

As one of the most important rare-earth oxides, ceria ($CeO_2$) has attracted a great deal of research attention due to its high oxygen storage capacity (OSC) and good redox properties [1-3]. Because of these unique characteristics, $CeO_2$ has been widely used as environmental catalysts for the removal of harmful pollutants from exhaust gases, such as oxidation of low-concen-

tration of CO [4], selective reduction of $NO_x$ with $NH_3$ [5], and oxidation of volatile organic compounds (VOC) [6,7]. The catalytic activity of $CeO_2$ is believed to originate from the reversible transformation between $Ce^{4+}$ and $Ce^{3+}$ and affected by various structural factors [8-10], including high surface area, preferential exposure of reactive facets and oxygen vacancy defects. However, pure $CeO_2$ deactivates seriously at an elevated temperature due to the decline of surface area and OSC. In order to maintain the OSC and enhance the catalytic activity and thermal stability of $CeO_2$, $CeO_2$-based composite oxides by combining ceria with other low-valence metal oxides have been widely studied. Importantly, due to the synergistic effect between the two components, $CeO_2$-based composite oxides exhibit a remarkable catalytic activity that is comparable with or even superior to that of noble metal-based catalysts in some catalytic reactions [11,12].

So far, a remarkable process has been developed for the synthesis of $CeO_2$-based composite oxides, including $CeO_2$–$CuO_x$ [13], $CeO_2$–$ZnCo_2O_4$ [14], $CeO_2$–$CoO_x$ [15], $CeO_2$–$MnO_x$ [16], $CeO_2$–ZnO [17], $CeO_2$–$Fe_2O_3$ [18], and $CeO_2$–$ZrO_2$ systems [19]. Taking the $CeO_2$–CuO catalyst as a typical example, the improved catalytic activity is closely related to the synergistic interaction between copper and ceria, which promotes the exchange of charges between $Ce^{4+}/Ce^{3+}$ and $Cu^{2+}/Cu^{+}$ and leads to faster oxidation and reduction than that of the corresponding independent forms. The formation of highly-dispersed copper species promotes the adsorption of CO molecules, while the presence of oxygen vacancies provided by $CeO_2$ can in turn create active oxygen in the oxidation reactions [12,13]. Therefore, the creation of two-phase interfaces as numerous as possible and, thus, the facilitation of synergistic interaction between two components are necessary to optimize the catalytic performances. The unique structure and texture of $CeO_2$-based catalysts is also associated with high activity and stability in the catalytic reaction. For instance, rod-like $CeO_2$–CuO catalysts with highly dispersed copper oxide clusters as active species had been reported to exhibit superior activity toward CO oxidation in contrast with commonly used $CeO_2$/CuO composite catalysts [13]. Consequently, the construction of ceria-based composite oxides with pore features, hollow structure or/and hierarchical architecture, which possess excellent redox properties and abundant oxygen vacancies, will be favorable for the enhancement of catalytic activity toward CO oxidation.

$CeO_2$-based hybrid oxides with hollow structure can be synthesized by a sacrificial-template method based on interfacial oxidation–reduction under mild conditions. For example, $Mn_3O_4$/$CeO_2$ hybrid nanotubes were created by a template-based process involving a redox reaction between the cryptomelane-type manganese oxide nanowire template and $Ce(NO_3)_3$ [20]. Ce–Mn nanotubes were also fabricated by treating $Ce(OH)CO_3$ templates with aqueous $KMnO_4$ solution and subsequent selective washing with $HNO_3$ to remove the residual $Ce(OH)CO_3$ [21]. In another case, well-dispersed $MnO_2$@$CeO_2$–$MnO_2$ and $CeO_2$–$CuO_x$ composite hollow spheres were synthesized through a facile reflux method using carbon spheres as sacrificial templates. The obtained material showed a high catalytic activity for CO oxidation [16,22]. In addition, porous/hollow $CeO_2$-based composite oxides with high surface area can be prepared through heat treatment of suitable cerium-containing precursors. Typically, uniform porous $Ce_{1-x}Zn_xO_{2-\delta}$ solid-solution nanodisks were synthesized by thermal decomposition of the as-prepared Ce–Zn precursor and exhibited excellent activity for removing CO [17]. $CeO_2$–ZnO composite hollow microspheres were fabricated via annealing of a precursor of amorphous zinc–cerium citrate hollow microspheres and presented excellent catalytic activity in CO oxidation [23]. Porous $CeO_2$:$Cu^{2+}$ materials with a tunable surface area were prepared through the thermolysis of a nanosized $CeCu(BTC)(H_2O)_6$ precursor [24]. Impressively, $Ce_2(SO_4)_3$ was employed as the precursor to synthesize mesoporous $CeO_2$–CuO bimetal oxide nanorods without the need for additional heat treatment, and the resultant sample exhibited enhanced catalytic activity in the oxidation of CO [25]. Otherwise, as a special composite structure, heterogeneous core@shell structures are believed to integrate the function of individual nanocrystals and induce the unique synergetic catalytic activities. For instance, $ZnCo_2O_4$@$CeO_2$ core@shell spheres [14] and $Co_3O_4$@$CeO_2$ core@shell cubes [26] with tunable $CeO_2$ shell thickness were prepared by a facile self-assembly method and exhibited promising performance in the catalytic oxidation of CO. Consequently, a suitable choice of templates or cerium-containing precursors and the control of the various factors that govern the morphology, texture and physico-chemical properties, provide a promising approach to fabricate $CeO_2$-based mixed oxide with various nanostructures. However, compared with pure $CeO_2$, it remains a challenge to synthesize $CeO_2$-based mixed oxides with well-defined morphology, tunable chemical composition and distribution, and desirable physico-chemical properties.

Herein, we report a general approach to fabricate uniform $CeO_2$–$MO_x$ (M = Cu, Co, Ni) composite yolk–shell nanospheres with highly dispersed $MO_x$ species, in which $CeO_2$ yolk–shell nanospheres were first constructed by non-equilibrium heat treatment of a Ce-CPCSs precursor and subsequent treatment with $M(CH_3COO)_2$ in a solvothermal process. Due to the well dispersion of $MO_x$ and the close contact between $CeO_2$ and $MO_x$, the resultant nanospheres exhibited improved catalytic activity in the oxidation of CO.

## Results and Discussion

### Formation and characterization

The synthetic mechanism for the $CeO_2$–$MO_x$ yolk–shell nanospheres is illustrated in Figure 1. First, according to the reported method [27], well-dispersed Ce-CPCSs with uniform size were synthesized on the basis of the integration of coordination chemistry with anti-solvent effects for synchronized precipitation. Second, the resultant Ce-CPCSs served as the precursor to produce $CeO_2$ yolk–shell nanospheres by non-equilibrium heat treatment with a proper heating rate. Heterogeneous contraction, caused by non-equilibrium heat treatment process, is regarded as a promising and effective approach to controllably design hollow structures with single and multilevel shells. The complexity of the shell structures is generally determined by the difference between the cohesive force ($F_c$) and the adhesive force ($F_a$) created by a proper temperature ramping rate [28-30]. In the early stages of heat treatment, at a high heating rate, a temperature gradient ($\Delta T$) along the radial direction leads to the generation of a dense $CeO_2$ shell at the surface of the Ce-CPCS core (stage I). Then, heterogeneous contraction takes place because the balance between the opposite forces $F_c$ and $F_a$ is disturbed. When $F_c > F_a$ at a high $\Delta T$, the inner core contracts inward and detaches from the preformed outer shell (stage II). During further annealing, the inner core shrinks into a solid structure and consequently $CeO_2$ yolk–shell spheres form (stage III). Upon solvothermal treatment, $M(CH_3COO)_2$ is hydrolyzed to $M(OH)_2$ and subsequently transformed into $MO_x$ and finally deposited onto the surface of $CeO_2$ yolk–shell spheres, leading to the formation of $CeO_2$−$MO_x$ composite yolk–shell spheres.

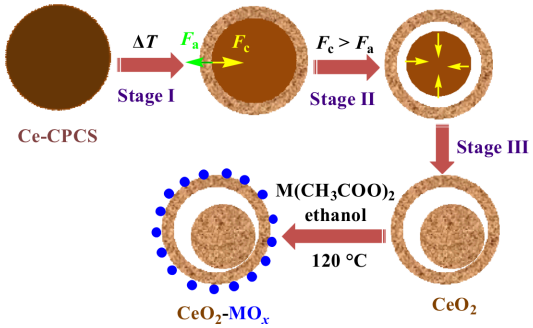


**Figure 1:** Schematic illustration of the formation of $CeO_2$–$MO_x$ composite yolk–shell nanospheres.

The morphology of the obtained samples was investigated by using scanning electron microscopy (SEM) and transmission electron microscopy (TEM). The as-synthesized Ce-CPCSs pre-

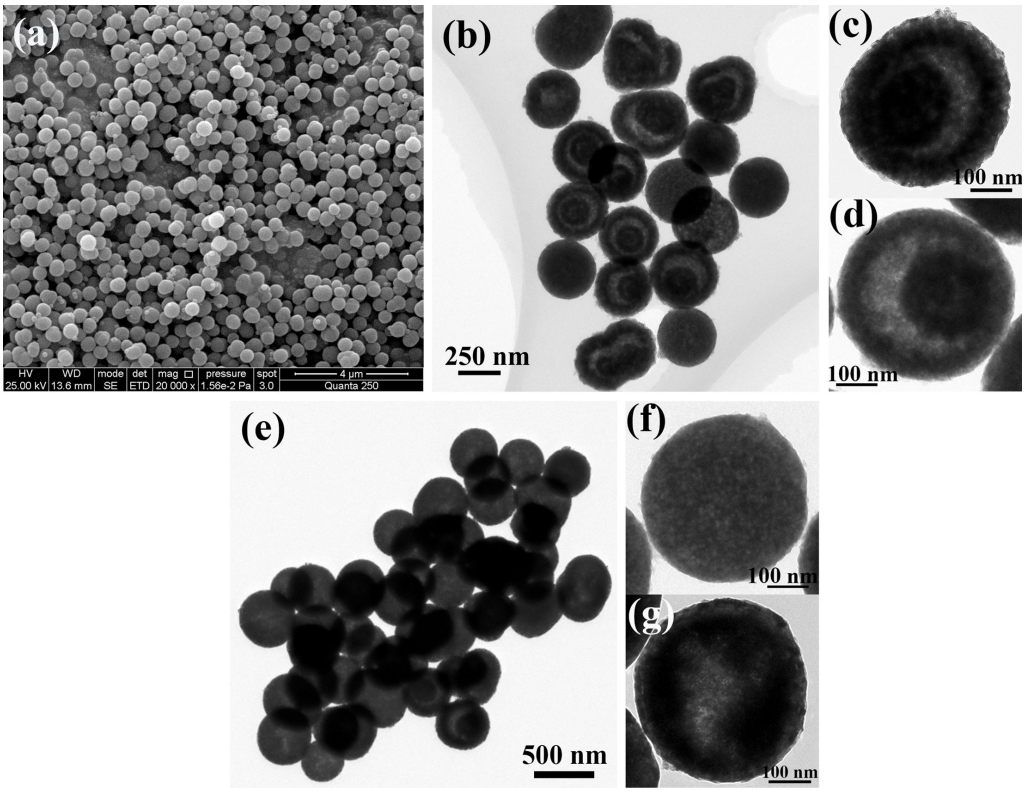


**Figure 2:** SEM image of Ce-CPCSs (a) and TEM images of (b–d) the $CeO_2$ yolk-shell nanospheres (heating rate 8 °C/min) and of (e–g) solid nanospheres (heating rate 2 °C/min).

cursor exhibits a well-dispersed solid spherical structure in the range of 400–500 nm (Figure 2a). It has been reported that, during the heating process, the calcination temperature and time is correlated with the crystalline structure of the as-obtained oxides, while a proper heating rate is necessary for the controllable synthesis of hollow structures with different multilevel interiors [30]. In our present work, when the Ce-CPCSs precursor was calcined at 500 °C with a heating rate of 8 °C/min, most of the obtained $CeO_2$ nanostructures present a yolk–shell spherical morphology with a shell thickness of about 50 nm (Figure 2b–d). In contrast, at a low heating rate of 2 °C/min, the Ce-CPCS spheres were almost homogeneously heated from the surface to the center and resulted in the formation of porous solid spheres along with some hollow structures (Figure 2e–g).

After further reaction between the yolk–shell structured $CeO_2$ and $Cu(CH_3COO)_2$ at 120 °C, the resultant $CeO_2$–$CuO_x$ composites still maintained the yolk–shell morphology without any obvious change after the harsh solvothermal treatment. The morphology of the $CeO_2$–$CuO_x$ yolk–shell spheres can be observed from TEM images in Figure 3. The strong contrast between outer shell and inside cavity indicates the hollow structure of the spheres. Besides, the size of $CeO_2$–$CuO_x$ composite yolk–shell nanospheres ranges from 400 to 500 nm with a shell thickness of approximately 50 nm (Figure 3b). The high-resolution TEM image is displayed in Figure 3c. The lattice fringe spacing of 0.31 nm and 0.27 nm can be indexed to the (111) and (200) crystal planes of face-centered-cubic fluorite-type $CeO_2$, respectively. No lattice spacing can be corresponded to Cu species. In the corresponding selected-area electron diffraction (SAED) pattern in Figure 3d only the diffraction rings belonging to $CeO_2$, indicative of a polycrystalline structure, can be recognized. This result is similar to the previously reported literature [22]. Energy-dispersive X-ray (EDX) analysis was

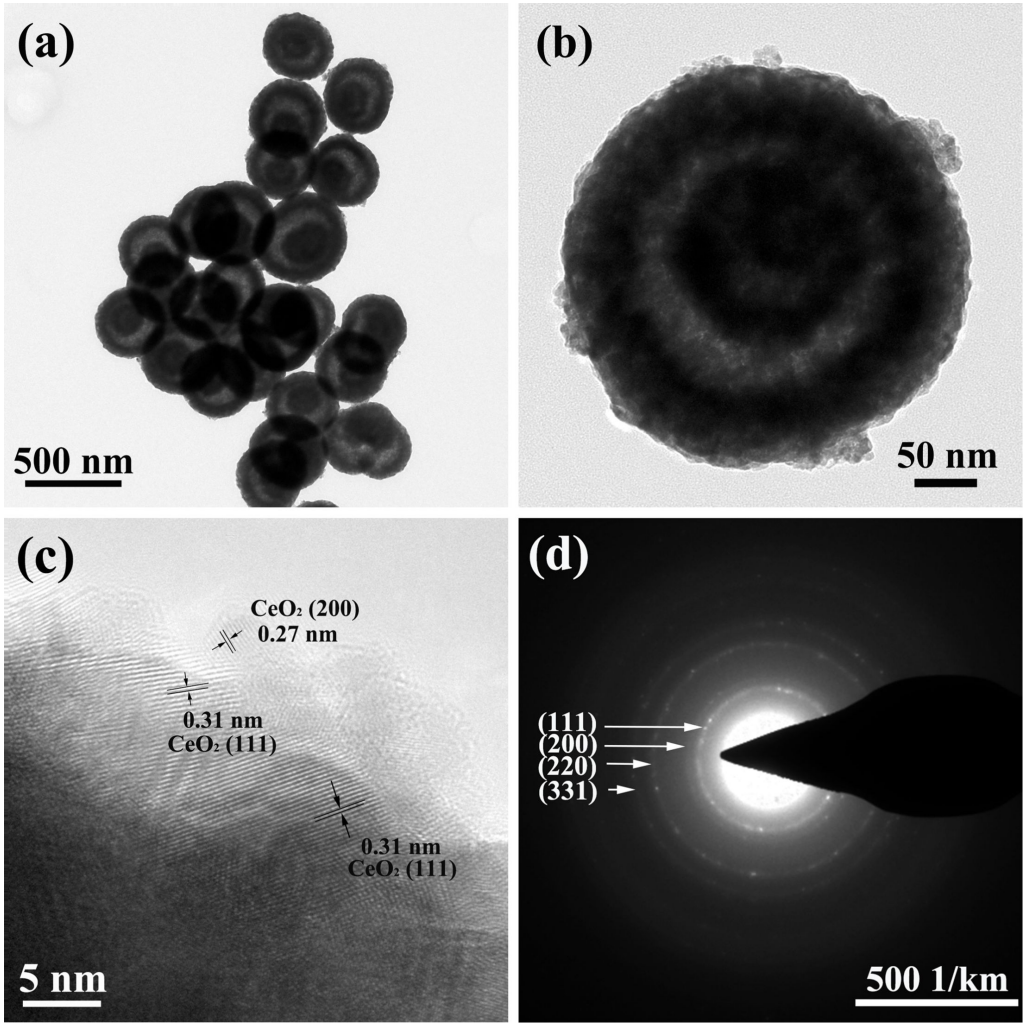


**Figure 3:** Low-magnification TEM images (a, b), high-magnification TEM image (c) and the SAED pattern (d) of the $CeO_2$−$CuO_x$ composite yolk-shell nanospheres.

employed to further investigate the elemental distribution of Ce and Cu species in the yolk–shell nanospheres. In Figure 4, the elements Ce, Cu, and O are represented by yellow, red, and green colors, respectively. A uniform distribution of Ce, Cu, and O in each yolk–shell sphere, which is favorable for the synergistic interaction between $CeO_2$ and $CuO_x$, can clearly be seen.

Ce–Co and Ce–Ni composite oxide nanostructures were prepared by a similar solvothermal process in which $CeO_2$ yolk–shell nanospheres were mixed with $Co(CH_3COO)_2$ or $Ni(CH_3COO)_2$ in ethanol solution. Spherical yolk–shell structures in the range of 400–500 nm are clearly observed in the TEM images (Figure 5a,b,d,e). The coexistence of Ce and Co or Ni is further confirmed by the EDX spectra (Figure 5c,f). These results indicate the versatility of this synthesis approach in the preparation of $CeO_2$-based transition-metal mixed-oxide nanostructures. Based on this synthesis method, other $CeO_2$-based composite oxides with various nanostructures can be expected to be fabricated through the pre-formation of $CeO_2$ or $CeO_2$-based solid solution with different morphologies and the subsequent decoration of highly dispersed transition-metal oxide cluster species.

Information about crystallinity and phases of the samples were obtained from X-ray diffraction (XRD) analysis. Figure 6a displays the XRD patterns of the as-synthesized $CeO_2$–$MO_x$

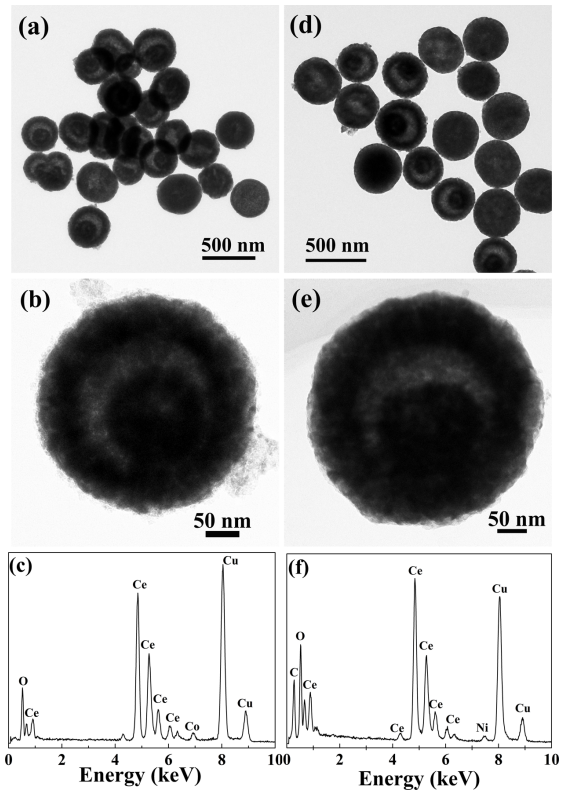


**Figure 5:** TEM images and the corresponding EDX patterns of the synthesized $CeO_2$–$CoO_x$ (a–c) and $CeO_2$–NiO (d–f) composite yolk–shell nanospheres.

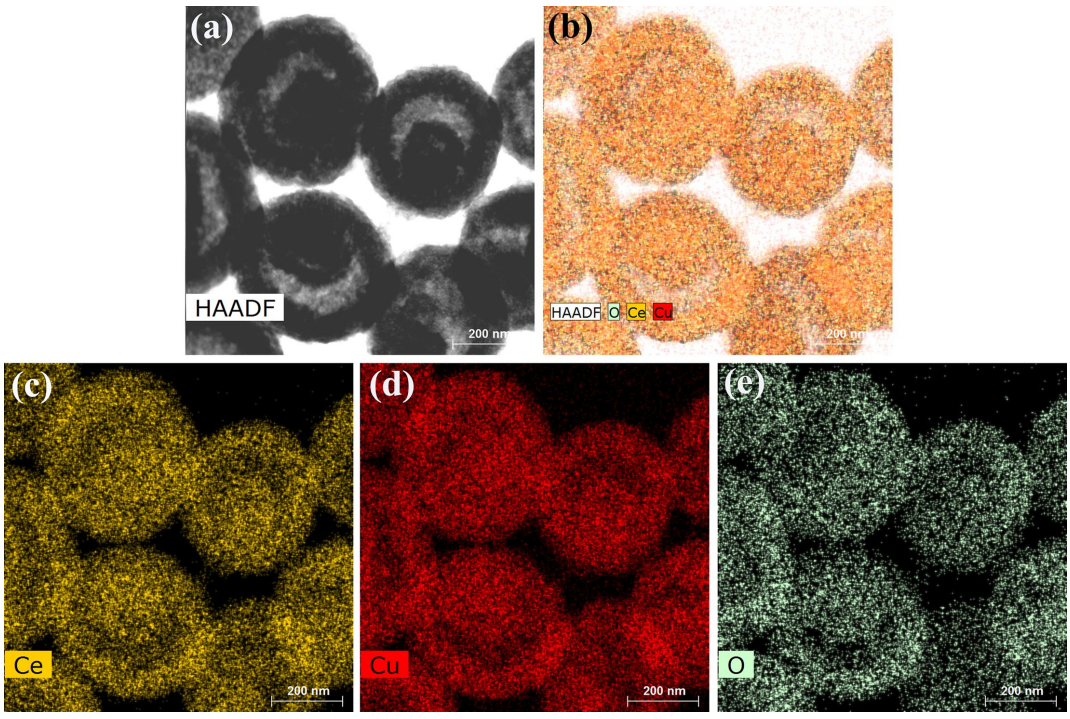


**Figure 4:** TEM image (a) and its mapping analysis (b–e) of the $CeO_2$–$CuO_x$ composite yolk–shell nanospheres.

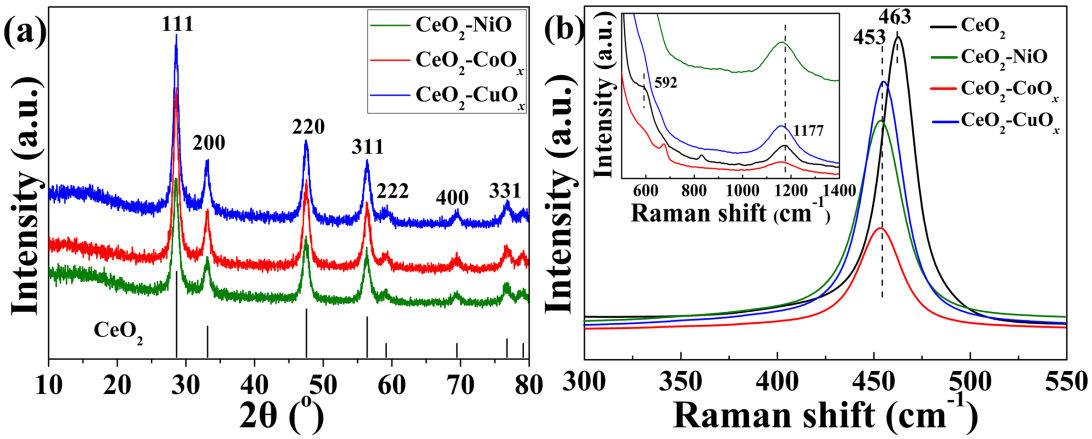


**Figure 6:** XRD patterns (a) and Raman spectra (b) of the as-synthesized $CeO_2$–$MO_x$ composite yolk–shell nanospheres.

nanospheres. All diffraction peaks can be assigned to the fluorite-like cubic phase of $CeO_2$ (JCPDS no. 34-0394). No diffraction peaks can be indexed to the $MO_x$ structure. The results indicate the high dispersion of $MO_x$ species onto the surface of $CeO_2$ or/and the introduction of M cations into the $CeO_2$ lattice.

The Raman spectra of the $CeO_2$–$MO_x$ yolk–shell spheres are illustrated in Figure 6b. All of the spectra reveal a main band at 450–465 $cm^{-1}$, which can be assigned to the $F_{2g}$ mode of the fluorite structure of $CeO_2$. Compared to pure $CeO_2$, the peak intensity of the $CeO_2$–$MO_x$ composite spheres decreases and the peak position shifts from 463 to 453 $cm^{-1}$. The peak shift depends on various parameters, including the crystal defects, oxygen vacancies, phonon confinement, and inhomogeneous strain related to the reduced ceria [31,32]. Herein, the shift can be related to the interaction between the $MO_x$ species and $CeO_2$ surface, which leads to lengthening and weakening of the M–O bond by sharing oxygen at the interface [29,30]. In addition, the incorporation of dopants can also result in shifts of the peak positions. This is, e.g., because the ion radius of $M^{2+}$ ($Cu^{2+}$ = 0.72 Å, $Co^{2+}$ = 0.79 Å, $Ni^{2+}$ = 0.83 Å) is much smaller than that of $Ce^{4+}$ (1.01 Å). Also, when a small number of $M^{2+}$ is embedded into the $CeO_2$ lattice and replaces $Ce^{4+}$, the Raman band shifts to lower wavenumbers because additional oxygen vacancies form to compensate for the valence mismatch between $M^{2+}$ and $Ce^{4+}$ ions [31]. Additionally, the weak peaks of pure $CeO_2$ at 592 and 1177 $cm^{-1}$ can be assigned to the D (defect-induced mode) and 2LO (second-order longitudinal optical mode) bands, respectively, which indicate the amount of surface oxygen vacancies [17]. The bands become more pronounced and shifts to lower wavenumbers for $CeO_2$–$MO_x$ samples. It appears that $CeO_2$–$MO_x$ samples, especially $CeO_2$–$CuO_x$ and $CeO_2$–NiO, generate more surface oxygen vacancies than pure $CeO_2$.

In order to obtain detailed information about the chemical bonding states of the as-prepared $CeO_2$–$MO_x$ yolk-shell nanospheres, X-ray photoelectron spectroscopy (XPS) analyses were carried out and the results are shown in Figure 7. As shown in Figure 7a, all samples exhibit similar profiles in the Ce 3d spectral region, which clearly represents a typical Ce(IV) 3d spectrum. Peaks centered at 882.1, 888.6, and 898.1 eV can be assigned to Ce(IV) $3d_{5/2}$, while peaks located at 900.5, 907.1, and 916.3 eV can be indexed to Ce(IV) $3d_{3/2}$, respectively [12,20]. In the O 1s spectra in Figure 7b, two peaks marked as $O_\alpha$ and $O_\beta$ are clearly identified. According to the literature, the main peak $O_\alpha$ at a binding energy of 529 eV is corresponding to lattice oxygen, while the shoulder peak $O_\beta$ at a binding energy of 531.3 eV is ascribed to defective or adsorptive oxygen species, such as low-coordinated oxygen atoms, chemisorbed oxygen, or hydroxy groups [12]. It is well-accepted that $O_\beta$ species are more active than $O_\alpha$ species due to their higher mobility. With the stronger $O_\beta$ peak, the $CeO_2$–$MO_x$ samples are expected to be richer in surface-active oxygen and have a better capacity for oxygen storage. In the Cu 2p spectrum (Figure 7c), two pronounced peaks at about 932.6 and 952.3 eV can be attributed to Cu $2p_{3/2}$ and Cu $2p_{1/2}$ of Cu(I), respectively, whereas a broad shake-up peak observed at around 946 eV can be assigned to the presence of Cu(II) [33]. It is therefore clear that the $CeO_2$–$CuO_x$ sample contains coexisting $Cu^+/Cu^{2+}$ oxidation states. In the Co 2p spectrum (Figure 7d), two strong peaks at 780.3 eV assigned to Co $2p_{3/2}$ and 796.3 eV to Co $2p_{1/2}$, along with two shake-up peaks at around 785.6 and 791 eV, are observed, indicating the coexistence of Co(II) and Co(III) in the $CeO_2$–$CoO_x$ sample. It has been reported that the oxidation state of Co can be distinguished by the binding energy and the intensity of shake-up satellites of the Co 2p photo-peak. Generally, $Co^{2+}$ shows two obvious shake-up satellites at around 785 and 802 eV, while pure $Co^{3+}$ displays only a very

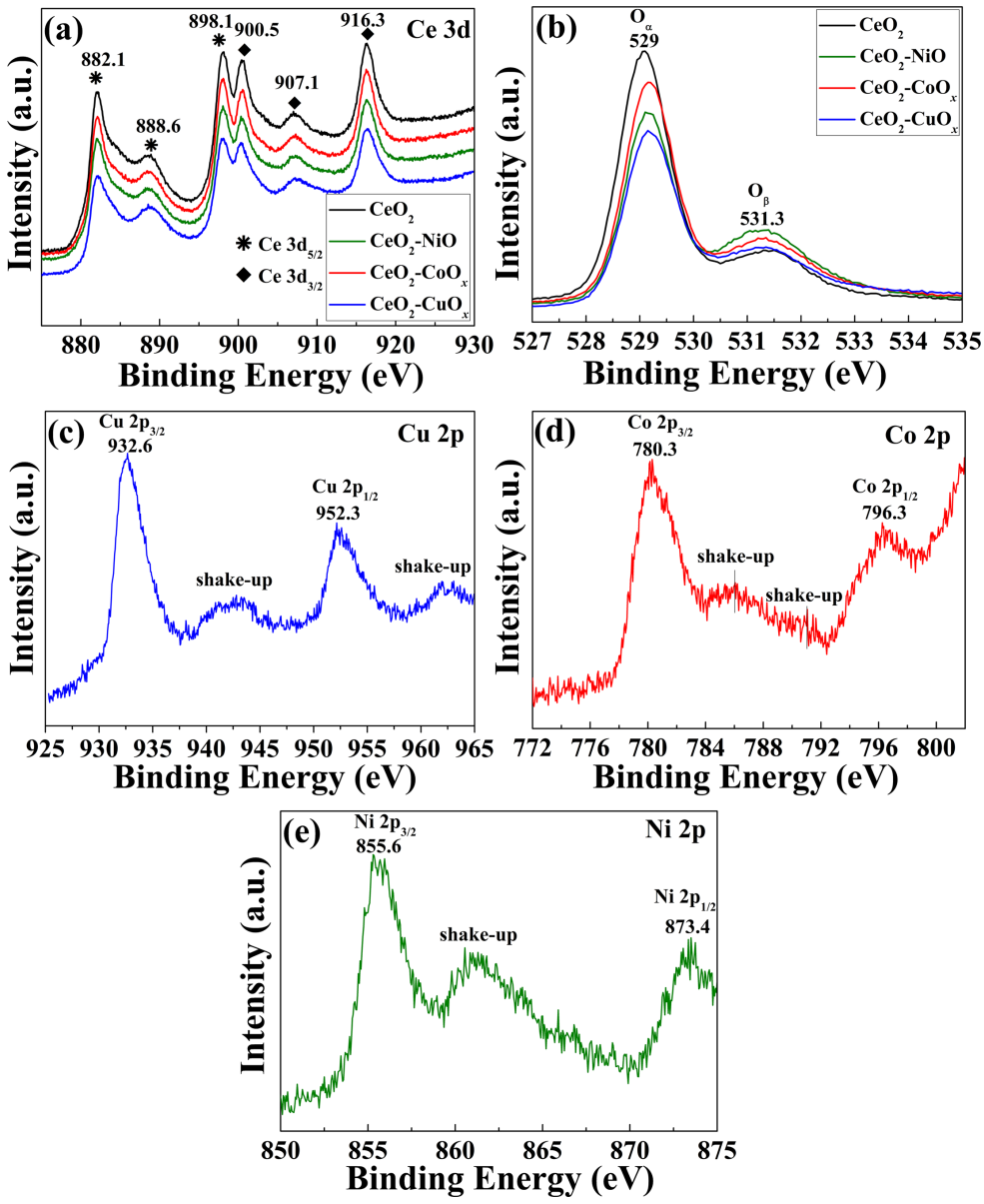


**Figure 7:** XPS spectra of Ce 3d (a), O 1s (b), Cu 2p (c), Co 2p (d) and Ni 2p (e) of the as-synthesized $CeO_2$–$MO_x$ composite yolk–shell nanospheres.

weak shake-up peak at about 791 eV. If $Co^{2+}/Co^{3+}$ oxidation states coexist, a plateau in the range of 783–792 eV will be observed instead of two distinct shake-up peaks [31,34]. In Ni 2p spectrum of the $CeO_2$–NiO sample (Figure 7e), the binding energies at 855.6 and 873.4 eV are ascribed to the characteristics Ni $2p_{3/2}$ and Ni $2p_{1/2}$ signals of Ni(II), while the peak at around 861.1 eV is the shake-up peak at the high-energy side of the Ni $2p_{3/2}$ edge [31].

Additionally, direct quantification of surface concentration ratio of M has been estimated by the integrated intensities of the M 2p and Ce 3d XPS peaks. As shown in Table 1, the surface M/(M + Ce) ratio calculated from XPS data is 37%, 22% and 28% for $CeO_2$–$CuO_x$, $CeO_2$–$CoO_x$ and $CeO_2$–NiO, respectively. Compared with 11.3%, 8.3% and 6.6% for the actual concentration measured by inductively coupled plasma mass spec-

**Table 1:** Chemical composition of the $CeO_2$–$MO_x$ composite yolk–shell nanospheres calculated from ICP-MS and XPS analyses.

| samples | $CeO_2$–CuO | $CeO_2$–$CoO_x$ | $CeO_2$–NiO |
|---|---|---|---|
| actual M/(M + Ce) ratio (atom %)[a] | 11.3 | 8.3 | 6.6 |
| surface M/(M + Ce) ratio (atom %)[b] | 37 | 22 | 28 |

[a]From ICP-MS analysis; [b]from XPS analysis.

trometry (ICP-MS) analysis, the surface concentration is higher than the actual concentration, which indicates the surface enrichment of $MO_x$ species. The high concentration of $MO_x$ species on the $CeO_2$ surface may result in the enhanced catalytic activity of the as-synthesized $CeO_2$–$MO_x$ samples.

In order to further understand the effect of the interaction between $CeO_2$ and $MO_x$ on the redox properties of these binary oxides, hydrogen temperature-programmed reduction ($H_2$-TPR) analysis was performed on the various $CeO_2$–$MO_x$ composite yolk–shell nanospheres. As displayed in Figure 8, pristine $CeO_2$ shows a clear reduction peak at 540 °C, which is attributed to the reduction of surface-oxygen species (capping oxygen). After the introduction of the $CuO_x$ phase, the surface-reduction peak is changed significantly and new peaks appear below 300 °C. For the $CeO_2$–$CuO_x$ composite yolk–shell nanospheres, two major reduction peaks are observed. The wide low-temperature band centered at 179 °C originates from the highly dispersed $CuO_x$ clusters, while the sharp high-temperature peak located at 200 °C is due to the strong interactions in the Cu–[O]–Ce structure [13]. In general, commercial $Cu_2O$ and pure CuO synthesized using a conventional precipitation method exhibit a $H_2$ consumption peak in the range of 240–300 °C, related to the reduction in the pure bulk $CuO_x$ phase [25,35]. For comparison, the binary Ce–Cu oxide shows relatively low reducibility compared to pure ceria and copper oxides due to the significant interaction between the two phases.

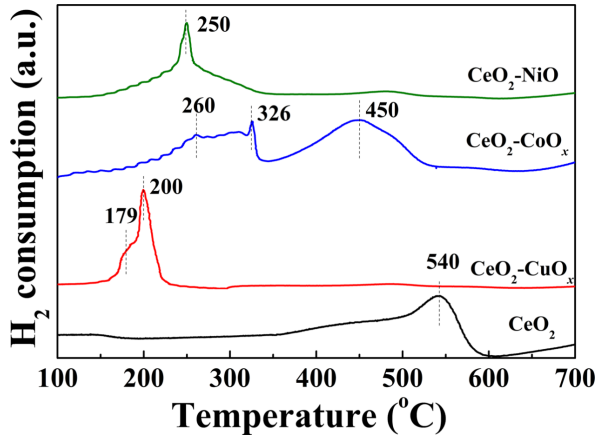


**Figure 8:** $H_2$-TPR profiles of as-prepared $CeO_2$, $CeO_2$–$CuO_x$, $CeO_2$–$CoO_x$ and $CeO_2$–NiO yolk–shell nanospheres.

In the case of $CeO_2$–$CoO_x$ sample, three reduction peaks are clearly displayed. Two weak peaks are located at relatively low temperatures of 260 and 326 °C, while the other board one is centered at 450 °C. According to the previous reports [11,36], the reduction peaks of $CeO_2$–$Co_3O_4$ catalysts in the $H_2$-TPR profiles can be generally divided into four temperature regions: α (< 240 °C), β (240–320 °C), γ (320–480 °C), and δ (480–700 °C). The peaks α and β are assigned to the reduction of adsorptive oxygen species on the surface and $Co^{3+}$ at the $CeO_2$–$Co_3O_4$ contact interface to $Co^{2+}$, respectively; while the peaks γ and δ are attributed to the reduction of $Co_3O_4$ and $Co^{2+}$ which interacted with the $CeO_2$ support to metal Co, respectively. On basis of these reduction patterns, the $H_2$ consumption peaks at 260 and 326 °C of the $CeO_2$–$CoO_x$ sample in our present work could be ascribed to the reduction of $Co^{3+}$ interacting with $CeO_2$ at the interface to $Co^{2+}$ and the reduction of $CoO_x$ weakly interacting with $CeO_2$ directly to metal Co, respectively. The broad reduction peak at 450 °C can be related with the reduction of $Co^{2+}$ interacting with $CeO_2$ to metal Co and $Ce^{4+}$ cations at the interface between $CoO_x$ and $CeO_2$. In addition, the pure $Co_3O_4$ bulk gets reduced at a high temperature of above 280 °C in the literature [6,11]. For the $H_2$-TPR profile of $CeO_2$–NiO sample, a sharp peak is clearly observed at around 250 °C, which can be due to the reduction of NiO cluster species weakly interacting with $CeO_2$ [37]. Comparatively, $Ni^{2+}$ ions were reduced to $Ni^0$ at the temperature of 330–430°C in pure NiO sample in the literature [38]. These results reveal that the strong interaction between the $MO_x$ species and $CeO_2$ is created at the two-phase interface of $CeO_2$−$MO_x$ composite yolk-shell nanospheres.

## Catalytic performance

CO oxidation as a model reaction was carried out to evaluate the catalytic performance of the $CeO_2$–$MO_x$ composite yolk–shell nanospheres and pristine $CeO_2$ for comparison. Figure 9 presents the catalytic activities for the above samples. As can be seen, the temperatures for 50% CO oxidation ($T_{50}$) of $CeO_2$–$CuO_x$, $CeO_2$–$CoO_x$ and $CeO_2$–NiO were 137, 167, and 185 °C, respectively, with a large temperature difference to pure $CeO_2$ (206 °C). Furthermore, complete CO conversion is obtained at 310 °C in the presence of pure $CeO_2$. This is in stark contrast to 160 °C with $CeO_2$–$CuO_x$, 203 °C with $CeO_2$–$CoO_x$ and 235 °C with $CeO_2$–NiO, respectively. Obviously, the $CeO_2$–$MO_x$ composite yolk–shell spheres showed much higher catalytic activity than pure $CeO_2$ yolk–shell spheres. Because the sample of solely $CeO_2$ has similar structural features to those of $CeO_2$–$MO_x$, the enhanced performance can be attributed to the decoration of $MO_x$ onto the $CeO_2$ surface and the strong synergistic interaction between $MO_x$ species and $CeO_2$. For comparison, a commercial $CeO_2$ material was measured under the same conditions for CO oxidation. Complete CO conversion was obtained at 367 and 221 °C over the naked and $CuO_x$-decorated commercial $CeO_2$ particles, respectively. By comparison, the yolk–shell nanospheres are more active than the commercial material under the same test conditions. The higher catalytic performances of our present samples could be related to the unique yolk–shell structure. During the catalytic

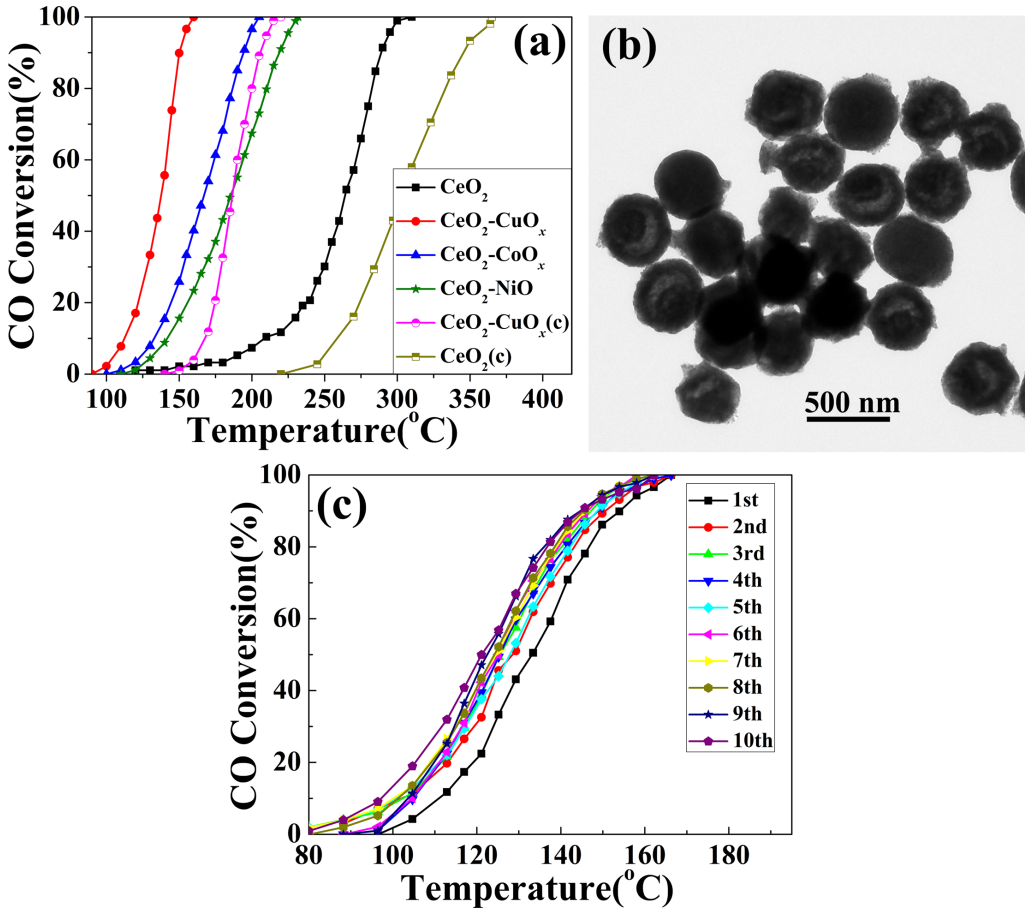


**Figure 9:** (a) CO conversions as a function of temperature for $CeO_2$ and $CeO_2$–$MO_x$ composite yolk–shell nanospheres, and naked and $CuO_x$-decorated commercial $CeO_2$ particles (denoted as $CeO_2$(c) and $CeO_2$−$CuO_x$(c), respectively), WHSV = 60000 mL $g^{-1}$ $h^{-1}$; (b) TEM image of the $CeO_2$–$CuO_x$ composite yolk–shell nanospheres after catalytic test; and (c) cycling test of the $CeO_2$–$CuO_x$ composite yolk–shell nanospheres for CO conversion.

process, CO molecules may easily diffuse into the cavities of the $CeO_2$–$CuO_x$ yolk–shell structure and then contact more active interface sites, thus enhancing the CO oxidation activity. Figure 9b shows the TEM image of the Ce–Cu binary oxides yolk–shell spheres after the catalytic test. The yolk–shell nanosphere morphology is largely retained during the catalytic oxidation, suggesting an excellent structural stability. To further explore the durability of the $CeO_2$–$MO_x$ catalyst, the $CeO_2$–$CuO_x$ sample was employed as a typical example and a cycling test was performed. As shown in Figure 9c, the $CeO_2$–$CuO_x$ sample still maintained 100% CO conversion at 165 °C after ten successive cycles. Interestingly, the catalytic activity in the 2nd to 10th run was not reduced, and even slightly higher than that in the first run. The possible reason can be attributed to an improvement of the oxidizability of $CuO_x$ species during the high-temperature treatment in the first run.

The initial concentration of $M(CH_3COO)_2{\cdot}xH_2O$ in the synthesis process played a significant role in catalytic performance for CO oxidation. By simply varying the amount of $M(CH_3COO)_2{\cdot}xH_2O$, a series of composite nanospheres was prepared to investigate the effects on the catalytic activity (the detailed synthesis is given in Experimental section). The CO conversion curves are shown in Figure 10. Each sample exhibits enhanced catalytic performance in comparison with naked $CeO_2$. For $CeO_2$–$CuO_x$, the corresponding samples were denoted as $CeO_2$–$CuO_x$–1, $CeO_2$–$CuO_x$–2, $CeO_2$–$CuO_x$–3 and $CeO_2$–$CuO_x$–4 obtained by addition of 0.01, 0.02, 0,04 and 0.08 mmol of $Cu(CH_3COO)_2{\cdot}H_2O$, respectively. $CeO_2$–$CuO_x$–1 sample exhibited a $T_{100}$ value of 235 °C (Figure 10a). The value of $T_{100}$ of $CeO_2$–$CuO_x$–2 sample sharply decreased to 145 °C. Upon a further increase of the initial concentration of $Cu(CH_3COO)_2{\cdot}H_2O$, the catalytic activity of the as-obtained samples deteriorated, with $T_{100}$ values of 160 °C for $CeO_2$–$CuO_x$–3 and 230 °C for $CeO_2$–$CuO_x$–4. Among the series of $CeO_2$–$CoO_x$ and $CeO_2$–NiO samples, the catalytic performance exhibited a similar trend (Figure 10b,c). $CeO_2$–$CoO_x$–2 and $CeO_2$−NiO−2 showed the optimal catalytic

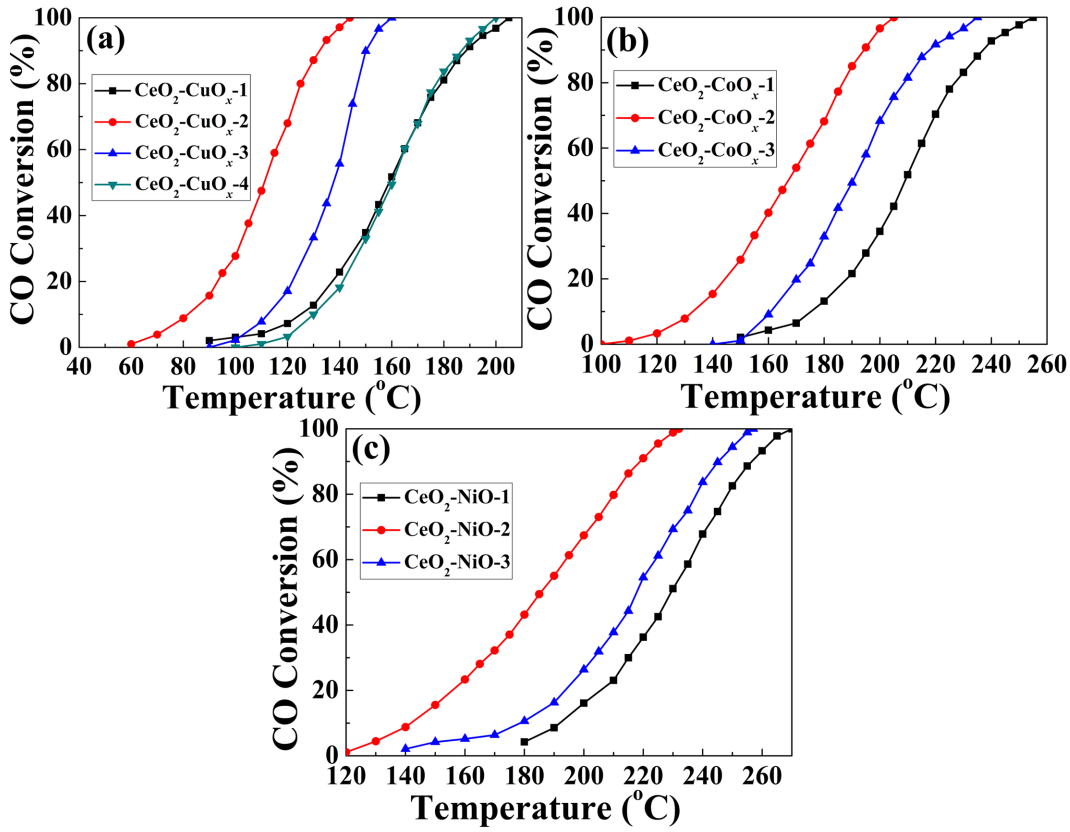


**Figure 10:** CO conversion as a function of temperature for $CeO_2$–$MO_x$ composite yolk–shell nanospheres obtained with different initial concentrations of $M(CH_3COO)_2{\cdot}xH_2O$: (a) $CeO_2$–$CuO_x$; (b) $CeO_2$–$CoO_x$ and (c) $CeO_2$–NiO.

performance, and $T_{100}$ values of 203 and 235 °C for $CeO_2$–$CoO_x$–2 and $CeO_2$–NiO–2, both of which were obtained with 0.04 mmol of $Co(CH_3COO)_2{\cdot}4H_2O$ and $Ni(CH_3COO)_2{\cdot}4H_2O$, respectively. The results indicate that the introduction of a proper amount of $MO_x$ species results in significantly higher catalytic activity of the $CeO_2$–$MO_x$ samples. However, an excessive amount of $MO_x$ introduced into $CeO_2$ may block the pore channels generated during the heating process and cover the active sites of $CeO_2$, leading to a decline of catalytic activity.

In principle, the catalytic process mainly involves the adsorption and desorption of gas molecules at the interface or on the surface during CO oxidation over metal-oxide catalysts. According to previously reported literature, the possible CO oxidation reaction mechanism over the ceria-based mixed oxides could be tentatively proposed as follows: CO + M–[O]–Ce–$\square_{vac}$ + 1/2 $O_2$ → [CO–M–O–Ce–O]* → $CO_2$ (g) + M–[O]–Ce–$\square_{vac}$, where M–[O]–Ce denotes a metal species incorporated into $CeO_2$, and $\square_{vac}$ denotes an oxygen vacancy [39]. Essentially, the interaction between $CeO_2$ and $MO_x$ is due to the lengthening and weakening of the M–O bond by sharing oxygen at the interface [40]. Therefore, the molecular oxygen activation and extraction preferentially takes place at the interface site between $MO_x$ and $CeO_2$. During CO oxidation over the $CeO_2$–$MO_x$ catalyst, $MO_x$ provides chemisorption sites for CO molecules, while $CeO_2$ traps oxygen molecules with oxygen vacancies and increases the concentration of surface oxygen due to its excellent oxygen storage capacity. In the CO oxidation process, oxygen atoms will transfer from molecular oxygen to the $MO_x$ clusters through the $CeO_2$, which is in close contact with $MO_x$ at the two-phase interface, remarkably promoting oxygen mobility on the surface of $CeO_2$–$MO_x$ composite and effectively facilitating molecular oxygen activation [41,42].

The $CeO_2$–$CuO_x$ catalyst exhibited much better activity than the other samples, indicating that the catalytic activity may be related with the intrinsic property of the doped metal and the metal-oxide interactions. For $MO_x$-decorated $CeO_2$ nanostructures, the enhanced redox properties at the interface sites play a key role in the superior catalytic efficiency in the oxidation reaction [33]. The charge balance of redox couples of $Cu^{2+}/Cu^{+}$ and $Ce^{4+}/Ce^{3+}$ ($Ce^{3+} + Cu^{2+} \leftrightarrow Ce^{4+} + Cu^{+}$) and the lowering of redox potentials of Cu species interacting with $CeO_2$ support could be responsible for the improved catalytic performance of the $CeO_2$–$CuO_x$ catalyst [43]. For Ce–Co and Ce–Ni binary

oxides, $Co^{3+}/Co^{2+}$ and $Ni^{3+}/Ni^{2+}$ charge pairs will also be balanced with $Ce^{4+}/Ce^{3+}$ pair at the two-phase interface [44]. Nevertheless, since the redox potentials follow the sequence of $Cu^{2+}/Cu^{+} << Co^{3+}/Co^{2+} \approx Ni^{3+}/Ni^{2+}$, Cu will be more effective than Co or Ni to achieve a charge balance with $Ce^{4+}/Ce^{3+}$, leading to more pronounced catalytic activity for CO oxidation [39,44]. In addition, the adsorption capacity for CO molecules is another important factor that influences the catalytic activities. Previous studies have shown that Ni and Co cations are less efficient for CO chemisorption than Cu cations, resulting in inferior CO oxidation activity [44,45]. As previously reported, the catalytic activities of 5% doped M–$CeO_2$ (M = Cu, Co and Ni) catalyst were evaluated, and the order of reaction rates in CO oxidation were Cu > Co > Ni > undoped [39,43], which is in accordance with the results of our present study.

## Conclusion

In summary, uniform $CeO_2$–$MO_x$ (M = Cu, Co, Ni) composite yolk–shell nanospheres have been successfully prepared by a general approach, consisting of the calcination of solid Ce-CPCSs precursor to produce $CeO_2$ yolk–shell nanospheres and the subsequent solvothermal treatment with $M(CH_3COO)_2$. Preliminary catalytic experiments indicate that the $CeO_2$–$MO_x$ composite nanospheres exhibited excellent catalytic activity toward CO oxidation. Additionally, cycling test confirms an excellent catalytic stability and durability during the CO oxidation process. The initial concentration of $M(CH_3COO)_2{\cdot}xH_2O$ in the synthesis process played a significant role in catalytic performance. The catalytic activity of the $CeO_2$–$CuO_x$-2 sample is comparable to the traditional noble-metal–$CeO_2$ system, yielding complete CO conversion at a relatively low temperature of 145 °C. A greatly enhanced performance of the composites in CO oxidation can be attributed to the incorporation of highly-dispersed $MO_x$ onto the $CeO_2$ surface and the strong synergistic interaction between $MO_x$ species and $CeO_2$. Additionally, the $CeO_2$–$CuO_x$ catalyst is more active than the $CeO_2$–$CoO_x$ and $CeO_2$–NiO catalysts for the CO oxidation, suggesting that the catalytic activity is mainly related to the intrinsic property of the doped metal and the metal-oxide interactions. It may be tentatively explained that the Co and Ni absorb less CO molecules less efficiently than Cu and are less effective in balancing charges with the $Ce^{4+}/Ce^{3+}$ pair. This synthesis approach could be further applied to create other $CeO_2$-based composite oxides with various nanostructures for a broad range of technical applications.

## Experimental

### Materials

Cerium(III) nitrate hexahydrate ($Ce(NO_3)_3{\cdot}6H_2O$), concentrated nitric acid ($HNO_3$, 68%), diethylene glycol (DEG), acetone, copper(II) acetate monohydrate ($Cu(CH_3COO)_2{\cdot}H_2O$), nickel(II) acetate tetrahydrate ($Ni(CH_3COO)_2{\cdot}4H_2O$), cobalt(II) acetate tetrahydrate ($Co(CH_3COO)_2{\cdot}4H_2O$) and absolute ethanol were purchased from Sinopharm Chemical Reagent Co. Ltd.. All the chemical reagents are analytically pure and used as received without further purification.

### Synthesis of $CeO_2$ yolk–shell nanospheres

The Ce-CPCSs were synthesized according to [27]. In a typical procedure, 0.109 g of $Ce(NO_3)_3{\cdot}6H_2O$ was dissolved in 5 mL of diethylene glycol under vigorous stirring. Subsequently, 2 mL of concentrated nitric acid and 35 mL of acetone were added to the above solution in sequence, and stirring was continued for another 30 min to form a clear solution. The resultant mixture was placed to a 50 mL Teflon-lined stainless steel autoclave and maintained at 100 °C for 10 h. After cooling to room temperature, the Ce-CPCSs were collected by centrifugation, washed with ethanol three times and oven-dried at 60 °C. The $CeO_2$ yolk–shell nanospheres were completed by thermal decomposition of the Ce-CPCSs at 500 °C for 4 h in air with a heating rate of 8 °C/min.

### Synthesis of $CeO_2$–$MO_x$ composite yolk–shell nanospheres

In a typical process, 0.04 mmol of $M(CH_3COO)_2{\cdot}xH_2O$ (M = Cu, Co, Ni) was dissolved in 16 mL of absolute ethanol under vigorous stirring. Then 50 mg of the as-prepared $CeO_2$ was dispersed into the above clear solutions under ultrasonification. Subsequently, the resultant homogeneous slurry was placed in a 25 mL Teflon-lined stainless steel autoclave and maintained at 120 °C for 12 h. Finally, the products were harvested by centrifugation and thoroughly washed with deionized water three times before being dried at 80 °C in an electric oven.

For comparison, a series of $CeO_2$–$MO_x$ samples were synthesized by addition of initial concentrations of $M(CH_3COO)_2{\cdot}xH_2O$ (M = Cu, Co, Ni), while other conditions were kept unchanged. For $CeO_2$–$CuO_x$ samples, 0.01, 0.02, 0.04 and 0.08 mmol of $Cu(CH_3COO)_2{\cdot}H_2O$ were introduced, the corresponding samples were named $CeO_2$–$CuO_x$–1, $CeO_2$–$CuO_x$–2, $CeO_2$–$CuO_x$–3 and $CeO_2$–$CuO_x$–4, respectively. For $CeO_2$–$CoO_x$ and $CeO_2$–NiO samples, 0.028, 0.04 and 0.052 mmol $M'(CH_3COO)_2{\cdot}4H_2O$ (M′ = Co, Ni) was added, the corresponding products were denoted $CeO_2$–$M'O_x$–1, $CeO_2$–$M'O_x$–2 and $CeO_2$–$M'O_x$–3, respectively.

### Characterization

Crystallographic phases and purity were investigated by X-ray diffraction (XRD) on a Bruker D8-Advance powder X-ray diffractometer with Cu Kα radiation (λ = 0.15418 nm). The morphologies and structures were examined by scanning elec-

tron microscopy (SEM) using a FEI Quanta$^{TM}$ 250 and transmission electron microscopy (TEM) using a FEI Tecnai G2 F20, equipped with an energy dispersive X-ray spectrometer (EDX) for elemental mapping. Raman spectra were carried out using a Bruker Senterra Raman spectrometer with an excitation laser of 532 nm. Surface analysis was obtained by an X-ray photoelectron spectroscopy (XPS, Thermo ESCALAB 250Xi) with Al Kα radiation. All binding energies were corrected for surface charging by use of the C 1s peak (284.8 eV) of adventitious carbon as reference. The M contents in $CeO_2$–$MO_x$ samples were analyzed by inductively coupled plasma mass spectrometry (ICP-MS, Agilent NWR 213-7900). Hydrogen temperature programmed reduction ($H_2$-TPR) experiment was performed on a PCA-1200 instrument, equipped with a thermal conductivity detector (TCD) to detect $H_2$ consumption. Typically, 50 mg of the sample was heated (10 °C/min) from room temperature to 700 °C in a 5 vol % $H_2$/Ar gaseous mixture with a flow rate of 30 mL/min.

### Catalytic tests

The activity measurements were carried out in a continuous flow fixed-bed microreactor at atmospheric pressure. In a typical experiment, 50 mg of catalyst with 500 mg silica sand was loaded into a stainless steel tube. A gas mixture of CO/$O_2$/$N_2$ (1:10:89) with a total flow rate of 50 mL/min flowed through the reactor, equivalent to a weight hourly space velocity (WHSV) of 60000 mL·g$^{-1}$·h$^{-1}$. The composition of the gas exiting from the reactor was monitored with an online infrared gas analyzer (Gasboard-3100, China Wuhan Cubic Co.) that can simultaneously detect CO, $CO_2$ and $O_2$. The CO conversion ratio was calculated based on the CO consumption and $CO_2$ formation.

## Acknowledgements

This work was financially supported by the Fundamental Research Funds for the Central Universities (Grant no. 2017QNA05).

## References

1. Montini, T.; Melchionna, M.; Monai, M.; Fornasiero, P. *Chem. Rev.* **2016,** *116,* 5987–6041. doi:10.1021/acs.chemrev.5b00603
2. Fang, S.; Xin, Y.; Ge, L.; Han, C.; Qiu, P.; Wu, L. *Appl. Catal., B: Environ.* **2015,** *179,* 458–467. doi:10.1016/j.apcatb.2015.05.051
3. He, L.; Li, J.; Feng, Z.; Sun, D.; Wang, T.; Li, R.; Xu, Y. *Appl. Surf. Sci.* **2014,** *322,* 147–154. doi:10.1016/j.apsusc.2014.10.100
4. Liu, D.; Li, W.; Feng, X.; Zhang, Y. *Chem. Sci.* **2015,** *6,* 7015–7019. doi:10.1039/C5SC02774H
5. Jiang, D.; Zhang, M.; Li, G.; Jiang, H. *Catal. Commun.* **2012,** *17,* 59–63. doi:10.1016/j.catcom.2011.10.020
6. Liotta, L. F.; Di Carlo, G.; Pantaleo, G.; Venezia, A. M.; Deganello, G. *Appl. Catal., B: Environ.* **2006,** *66,* 217–227. doi:10.1016/j.apcatb.2006.03.018
7. Liotta, L. F.; Ousmane, M.; Di Carlo, G.; Pantaleo, G.; Deganello, G.; Marcì, G.; Retailleau, L.; Giroir-Fendler, A. *Appl. Catal., A* **2008,** *347,* 81–88. doi:10.1016/j.apcata.2008.05.038
8. He, H.; Yang, P.; Li, J.; Shi, R.; Chen, L.; Zhang, A.; Zhu, Y. *Ceram. Int.* **2016,** *42,* 7810–7818. doi:10.1016/j.ceramint.2016.02.005
9. Shi, W.; Li, Y.; Hou, J.; Lv, H.; Zhao, X.; Fang, P.; Zheng, F.; Wang, S. *J. Mater. Chem. A* **2013,** *1,* 728–734. doi:10.1039/C2TA00504B
10. Lee, Y.; He, G.; Akey, A. J.; Si, R.; Flytzani-Stephanopoulos, M.; Herman, I. P. *J. Am. Chem. Soc.* **2011,** *133,* 12952–12955. doi:10.1021/ja204479j
11. Liotta, L. F.; Wu, H.; Pantaleoa, G.; Venezia, A. M. *Catal. Sci. Technol.* **2013,** *3,* 3085–3102. doi:10.1039/C3CY00193H
12. Qi, L.; Yu, Q.; Dai, Y.; Tang, C.; Liu, L.; Zhang, H.; Gao, F.; Dong, L.; Chen, Y. *Appl. Catal., B: Environ.* **2012,** *119–120,* 308–320. doi:10.1016/j.apcatb.2012.02.029
13. Wang, W.-W.; Du, P.-P.; Zou, S.-H.; He, H.-Y.; Wang, R.-X.; Jin, Z.; Shi, S.; Huang, Y. -Y.; Si, R.; Song, Q.-S.; Jia, C.-J.; Yan, C.-H. *ACS Catal.* **2015,** *5,* 2088–2099. doi:10.1021/cs5014909
14. Wang, F.; Wang, X.; Liu, D.; Zhen, J.; Li, J.; Wang, Y.; Zhang, H. *ACS Appl. Mater. Interfaces* **2014,** *6,* 22216–22223. doi:10.1021/am505853p
15. Zhen, J.; Wang, X.; Liu, D.; Wang, Z.; Li, J.; Wang, F.; Wang, Y.; Zhang, H. *J. Nano Res.* **2015,** *8,* 1944–1955. doi:10.1007/s12274-015-0704-3
16. Zhang, J.; Cao, Y.; Wang, C.-A.; Ran, R. *ACS Appl. Mater. Interfaces* **2016,** *8,* 8670–8677. doi:10.1021/acsami.6b00002
17. Zhong, S.-L.; Zhang, L.-F.; Wang, L.; Huang, W.-X.; Fan, C.-M.; Xu, A.-W. *J. Phys. Chem. C* **2012,** *116,* 13127–13132. doi:10.1021/jp3017826
18. Bao, H.; Chen, X.; Fang, J.; Jiang, Z.; Huang, W. *Catal. Lett.* **2008,** *125,* 160–167. doi:10.1007/s10562-008-9540-3
19. Liang, X.; Wang, X.; Zhuang, Y.; Xu, B.; Kuang, S.; Li, Y. *J. Am. Chem. Soc.* **2008,** *130,* 2736–2737. doi:10.1021/ja7109629
20. Guo, S.; Sun, W.; Yang, W.; Xu, Z.; Li, Q.; Shang, J. K. *ACS Appl. Mater. Interfaces* **2015,** *7,* 26291–26300. doi:10.1021/acsami.5b08862
21. Chen, G.; Rosei, F.; Ma, D. *Adv. Funct. Mater.* **2012,** *22,* 3914–3920. doi:10.1002/adfm.201200900
22. Zhang, J.; Gong, M.; Cao, Y.; Wang, C.-A. *RSC Adv.* **2015,** *5,* 95133–95139. doi:10.1039/c5ra16410a
23. Xie, Q.; Zhao, Y.; Guo, H.; Lu, A.; Zhang, X.; Wang, L.; Chen, M.-S.; Peng, D.-L. *ACS Appl. Mater. Interfaces* **2014,** *6,* 421–428. doi:10.1021/am404487b
24. Li, S.; Wang, N.; Yue, Y.; Wang, G.; Zu, Z.; Zhang, Y. *Chem. Sci.* **2015,** *6,* 2495–2500. doi:10.1039/C5SC00129C
25. Chen, G.; Xu, Q.; Yang, Y.; Li, C.; Huang, T.; Sun, G.; Zhang, S.; Ma, D.; Li, X. *ACS Appl. Mater. Interfaces* **2015,** *7,* 23538–23544. doi:10.1021/acsami.5b06495
26. Zhen, J.; Wang, X.; Liu, D.; Song, S.; Wang, Z.; Wang, Y.; Li, J.; Wang, F.; Zhang, H. *Chem. – Eur. J.* **2014,** *20,* 4469–4473. doi:10.1002/chem.201304109
27. Li, C. C.; Zeng, H. C. *J. Am. Chem. Soc.* **2012,** *134,* 19084–19091. doi:10.1021/ja307280v
28. Zhou, L.; Xu, H.; Zhang, H.; Yang, J.; Hartono, S. B.; Qian, K.; Zou, J.; Yu, C. *Chem. Commun.* **2013,** *49,* 8695–8697. doi:10.1039/C3CC43867H
29. Liu, L.; Zhang, X.; Liu, J. *Mater. Lett.* **2014,** *136,* 209–213. doi:10.1016/j.matlet.2014.08.062
30. Guan, J.; Mou, F.; Sun, Z.; Shi, W. *Chem. Commun.* **2010,** *46,* 6605–6607. doi:10.1039/C0CC01044H

31. Liu, X.; Han, L.; Liu, W.; Yang, Y. *Eur. J. Inorg. Chem.* **2014,** 5370–5377. doi:10.1002/ejic.201402570
32. Qiao, D.; Lu, G.; Guo, Y.; Wang, Y.; Guo, Y. *J. Rare Earths* **2010,** *28,* 742–746. doi:10.1016/S1002-0721(09)60192-7
33. Sudarsanam, P.; Hillary, B.; Mallesham, B.; Rao, B. G.; Amin, M. H.; Nafady, A.; Alsalme, A. M.; Reddy, B. M.; Bhargava, S. K. *Langmuir* **2016,** *32,* 2208–2215. doi:10.1021/acs.langmuir.5b04590
34. Gu, D.; Jia, C.-J.; Weidenthaler, C.; Bongard, H.-J.; Spliethoff, B.; Schmidt, W.; Schüth, F. *J. Am. Chem. Soc.* **2015,** *137,* 11407–11418. doi:10.1021/jacs.5b06336
35. Wang, X.; Liu, D.; Li, J.; Zhen, J.; Zhang, H. *NPG Asia Mater.* **2015,** *7,* e158. doi:10.1038/am.2014.128
36. Luo, J.-Y.; Meng, M.; Zha, Y.-Q.; Guo, L.-H. *J. Phys. Chem. C* **2008,** *112,* 8694–8701. doi:10.1021/jp800651k
37. Du, X.; Zhang, D.; Shi, L.; Gao, R.; Zhang, J. *J. Phys. Chem. C* **2012,** *116,* 10009–10016. doi:10.1021/jp300543r
38. Cho, H.; Lee, H.; Park, S.-M.; Choi, B.-H.; Kang, M. *J. Nanomater.* **2013,** *2013,* 640146. doi:10.1155/2013/640146
39. Park, Y.; Kim, S. K.; Pradhan, D.; Sohn, Y. *Chem. Eng. J.* **2014,** *250,* 25–34. doi:10.1016/j.cej.2014.03.070
40. Shapovalov, V.; Metiu, H. *J. Catal.* **2007,** *245,* 205–214. doi:10.1016/j.jcat.2006.10.009
41. Liu, W.; Sarofim, A. F.; Flytzani-Stephanopoulos, M. *Chem. Eng. Sci.* **1994,** *49,* 4871–4888. doi:10.1016/S0009-2509(05)80066-1
42. Pu, Z.-Y.; Liu, X.-S.; Jia, A.-P.; Xie, Y.-L.; Lu, J.-Q.; Lu, M.-F. *J. Phys. Chem. C* **2008,** *112,* 15045–15051. doi:10.1021/jp805389k
43. Bera, P.; Mitra, S.; Sampath, S.; Hegde, M. S. *Chem. Commun.* **2001,** 927–928. doi:10.1039/B101416L
44. Wang, S.-Y.; Li, N.; Luo, L.-F.; Huang, W.-X.; Pu, Z.-Y.; Wang, Y.-J.; Hua, G.-S.; Luo, M.-F.; Lu, J.-Q. *Appl. Catal., B: Environ.* **2014,** *144,* 325–332. doi:10.1016/j.apcatb.2013.07.037
45. Jia, A.-P.; Hu, G.-S.; Meng, L.; Xie, Y.-L.; Lu, J.-Q.; Luo, M.-F. *J. Catal.* **2012,** *289,* 199–209. doi:10.1016/j.jcat.2012.02.010

## License and Terms

This is an Open Access article under the terms of the Creative Commons Attribution License (http://creativecommons.org/licenses/by/4.0), which permits unrestricted use, distribution, and reproduction in any medium, provided the original work is properly cited.

The license is subject to the *Beilstein Journal of Nanotechnology* terms and conditions: (http://www.beilstein-journals.org/bjnano)

The definitive version of this article is the electronic one which can be found at: doi:10.3762/bjnano.8.241